Nano Research
2023, 16(1): 999–1008

ISSN 1998-0124 CN 11-5974/O4
https://doi.org/10.1007/s12274-022-4837-x

Research Article

# Cationic antibacterial metal nanoclusters with traceable capability for fluorescent imaging the nano–bio interactions

Yixiao Li[1], Shaohua Qu[1], Yumeng Xue[1], Lianbing Zhang[2], and Li Shang[1,3] (✉)

[1] *School of Materials Science and Engineering, Northwestern Polytechnical University, Xi'an 710072, China*
[2] *School of Life Sciences, Northwestern Polytechnical University, Xi'an 710072, China*
[3] *Northwestern Polytechnical University Chongqing Technology Innovation Center, Chongqing 400000, China*



**Received:** 13 June 2022 / **Revised:** 28 July 2022 / **Accepted:** 30 July 2022

## ABSTRACT

A thorough understanding of antimicrobial mechanism is of great importance for developing novel, efficient antibacterial agents. While cationic nanoparticles, such as metal nanoclusters (NCs), represent an attractive type of antibacterial nanoagents, their interactions with bacteria remains largely un-elucidated. Herein, we report the synthesis of cationic bovine serum albumin-protected AuAgNCs (cBSA-AuAgNCs), which exhibit both near-infrared (NIR) fluorescence properties and significant antimicrobial effects. With *E. coli* and *S. aureus* as the representative bacteria, we investigated the antimicrobial process of cBSA-AuAgNCs in real-time based on their intrinsic fluorescence properties via fluorescence imaging. Our results showed that these cBSA-AuAgNCs exert their antimicrobial effects primarily by attaching on the outer membrane of bacteria without obvious internalization, which is significantly different from the antibacterial process of negatively-charged metal NCs. Further mechanistic investigation showed that these cationic NCs will cause serious disruption to the bacterial membrane due to strong electrostatic interactions, which then leads to over accumulation of reactive oxygen species (ROS) that finally causes the bactericidal action. This study demonstrates the great potential of cationic luminescent metal NCs as novel, traceable antimicrobial agents, which also provides new tools for further understanding microbial interactions of nanomedicines.

## KEYWORDS

metal nanoclusters, antimicrobial agents, bacterial imaging, near-infrared fluorescence

## 1 Introduction

Bacteria-caused diseases and infections are serious threats to human health [1, 2]. For a long time, antibiotics have been harnessed as a useful weapon against pathogenic bacteria, but they have caused severe drug-resistance due to abuse [3, 4]. Recently, with the rapid development of nanotechnology, researchers have discovered that many nanomaterials hold great promises as new generation of antimicrobial agents, among which cationic nanoparticles exhibit superior sterilization capability [5–9]. On the one hand, nanoparticles with positive surface charges possess a strong affinity to negatively-charged bacterial phospholipids due to electrostatic interactions, which facilitates their further interactions with bacteria. On the other hand, nanoparticles could kill pathogenic bacteria through a synergistic effect of multiple mechanisms, which will result in a less tendency of developing drug resistance [10, 11]. It is noteworthy that despite many researches on the development of various cationic antibacterial nanoagents in the past decades, a thorough understanding of their antibacterial mechanism, especially interactions at the early stage of the antibacterial process, has not been achieved yet. The main barrier is the lack of robust means that enable real-time and *in situ* monitoring of the antimicrobial process. Unfortunately, traditional observation methods, such as scanning electron microscopy (SEM), transmission electron microscopy (TEM), and surface plasmon resonance (SPR), typically yield *ex-situ* information that may not well reflect what is happening in the realistic biological environment [12–14]. Therefore, it is necessary to develop new approaches for real time monitoring the nanomaterial–bacteria interactions, which will be of great significance to advance the development of novel, efficient antibacterial nanoagents.

In recent years, ultrasmall metal nanoclusters (NCs), composed of several to hundreds of metal atoms, have been found to possess interesting antimicrobial activity [15–18]. For instance, Xie et al. [15] reported that 6-mercaptohexanoic acid-protected AuNCs exhibit surprisingly high wide-spectrum antimicrobial activity, which is absent for their large counterpart, metal nanoparticles. Recently, we and other groups reported the synthesis of cationic AuNCs with strong antimicrobial effect and negligible drug resistance [19, 20]. These studies all suggest the great potential of metal NCs, especially cationic NCs, as novel antibacterial agents in theranostic applications. It is noteworthy that with an ultrasmall size of only a few nanometers and ultra-high surface reactivity, these metal NCs are expected to exhibit distinct biological behaviors [21–25]. For example, previous studies found that dihydrolipoic acid-protected AuNCs will accumulate on the mammalian cell membrane to trigger their subsequent cellular internalization [26], which is absent for large nanoparticles. Therefore, in order to guide the rational design of more efficient metal NC-based antibacterial agents and further advance their clinical applications, a clear mechanistic understanding of their interactions with microbes is necessary and important.

Address correspondence to li.shang@nwpu.edu.cn

Unlike large metal nanoparticles, metal NCs exhibit distinct fluorescence properties, including large Stokes shift, tunable emission wavelength, and good photostability [27–32]. These attractive fluorescence features make it possible to visualize the interactions of NCs with bacteria by the virtue of their intrinsic fluorescence in a simple and real-time manner [16]. Compared to monometallic NCs, bimetallic NCs usually exhibit better stability and tunable property. In the present work, we report the synthesis of cationic bovine serum albumin-protected AuAgNCs (cBSA-AuAgNCs), which exhibit both near-infrared (NIR) fluorescence properties and significant antimicrobial effects. By taking *E. coli* and *S. aureus* as the representative bacteria, we investigated the antimicrobial process of cBSA-AuAgNCs in real-time based on their intrinsic fluorescence property (Scheme 1). Our results clearly revealed that these cationic NCs primarily attach to the bacterial membranes and subsequently kill bacteria via membrane disruption and reactive oxygen species (ROS) generation. Unlike negatively-charged metal NCs, these cationic NCs do not show obvious internalization during the antibacterial process.

## 2 Materials and methods

### 2.1 Reagents

All chemicals used are of analytical grade. BSA, gold(III) chloride trihydrate ($HAuCl_4{\cdot}3H_2O$), and silver nitrate ($AgNO_3$) were from Sigma-Aldrich (Milwaukee, USA). Sodium sulfide nonahydrate ($Na_2S{\cdot}9H_2O$), sodium hydroxide (NaOH), N-(3-Dimethylaminopropyl)-N'-ethyl carbodiimide hydrochloride (EDC), and ethylenediamine dihydrochloride ($C_2H_8N_2{\cdot}2HCl$) were from Aladdin (Shanghai, China). Hoechst 33342 was from Invitrogen (Thermo Fisher Scientific Company). Propidium iodide (PI) was from Beijing Solarbio Science & Technology Company. Nile Red was from Sangon Biotech Company. DNA extraction kit and ROS test kit were from Beyotime Institute of Biotechnology. Cell Counting Kit-8 (CCK-8) was from Dojindo Molecular Technologies Company. In all preparations, deionized water (18.25 MΩ·cm, Molecular Company) was used.

### 2.2 Synthesis of cBSA-AuAgNCs

A typical synthesis of cBSA-AuAgNCs is described as follows. $AgNO_3$ (3.4 mg/mL, 1 mL) was added to BSA (250 mg in 9 mL $H_2O$) at room temperature. The solution was stirred for 1 h before NaOH (2 mol/L, 250 μL) was introduced slowly, and argon was then pumped into the solution for 30 min. Afterwards, $Na_2S$ (24 mg/mL, 600 μL) solution was slowly added and the solution turned to yellow. The mixture solution was stirred in the dark with argon pumped for another 16 h. During the reaction, the color of the solution slowly turned into greyish-green. Afterwards, the solution was purified by triple centrifugation filtration with a molecular weight cut-off (MWCO) of 30 kDa (Millipore, Amicon, Ultra-15) and re-dispersed in water. Then $HAuCl_4$ (10 mmol/L, 5 mL) was introduced to the prepared solution at 37 °C, and stirred for 2 min before NaOH (1 mol/L, 500 μL) was added. After reacting at 37 °C for 12 h, the color of the solution turned brown with red fluorescence. The obtained BSA-AuAgNCs were purified by triple centrifugation filtration (MWCO: 30 kDa) and re-dispersed in water for later use. To prepare cBSA-AuAgNCs, ethylenediamine dihydrochloride (2.5 mol/L, 5 mL) and EDC (40 mg) were further added to BSA-AuAgNCs solution (25 mg/mL, 5 mL). The mixture solution was stirred at room temperature for 2 h, purified by triple centrifugation filtration before re-dispersing in water, and finally freeze-drying for later use.

### 2.3 Instruments for characterization

Ultraviolet–visible (UV–vis) absorption spectra were recorded with a U-3900H spectrophotometer (Hitachi, Tokyo, Japan).

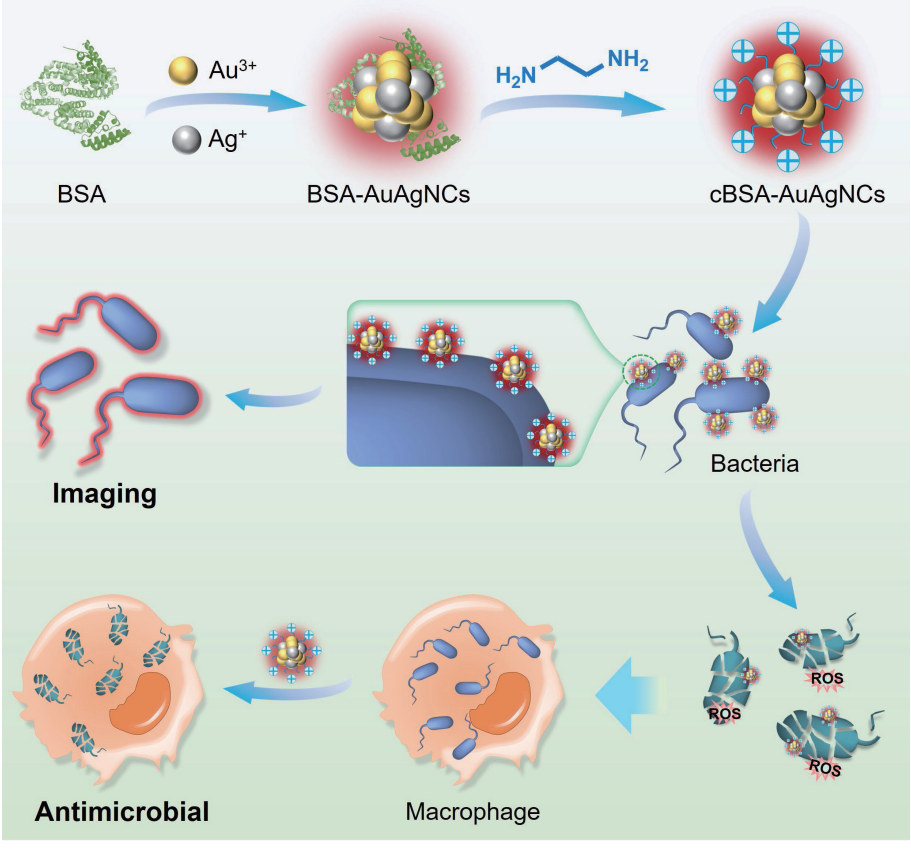


**Scheme 1** Schematic illustration of NIR fluorescent cBSA-AuAgNCs with good antimicrobial effect and their application for tracking the antibacterial process.

Fluorescence spectra were taken on a FLS 980 spectrofluorometer (Edinburgh Instruments, UK). Fluorescence lifetime spectra were taken with a DeltaFlex modular fluorescence lifetime system (Horiba, Kyoto, Japan). TEM was performed on a Tecnai $G^2$ F20 S-TWIN (FEI, Eindhoven, the Netherlands) equipped with a thermally assisted field-emission gun, which was operated at an accelerating voltage of 200 kV. TEM samples were prepared by spraying a dispersion of AuAgNCs onto a Cu grid covered by a holey carbon film. Zeta potential and dynamic light scattering (DLS) size were measured in water solution by Zetasizer Nano ZS (Malvern, UK). X-ray photoelectron spectroscopy (XPS) was carried out on an Axis Ultra DLD XPS spectrometer (Kratos, Manchester, UK), using Al K$\alpha$ X-ray radiation (1,486.6 eV) for excitation. All spectra were referenced to the C 1s peak at 284.8 eV. SEM images were taken from a NOVA450 SEM (FEI, Eindhoven, the Netherlands), and samples were prepared by spraying a dispersion of bacteria onto a Si wafer. Confocal fluorescence images were taken with a SP8 fluorescence confocal microscope (Leica, Germany).

### 2.4 Cell culture and cytotoxicity assay

The cytotoxicity of cBSA-AuAgNCs was assayed with mouse fibroblast cells (L929) and macrophage cells (Raw 264.7). Cells were cultured in Dulbecco's modified eagle medium (DMEM, Invitrogen, Carlsbad, California), supplemented with 10% fetal bovine serum and 1% penicillin and streptomycin under 37 °C and 5% $CO_2$. Cells were seeded into 96-well plates at a density of $1.0 \times 10^5$ cells/well in 200 μL culture medium and incubated for 24 h. Then the medium with different concentrations of cBSA-AuAgNCs was added to the 96-well plates and incubated for another 24 h. Six wells with only the complete medium were used as the control. Next, the medium was removed and 100 μL CCK-8 (5%) solution was added to each well. The absorbance at 450 nm was then read on a Microplate Reader (Tecan, Austria) and further analyzed. All experiments were conducted in triplicate.

### 2.5 Antibacterial test by the spread plate method

Both liquid and solid lysogeny broth (LB) culture mediums were used for antimicrobial test. Liquid LB culture medium was prepared by mixing 10 g NaCl, 5 g yeast extract, 10 g tryptone, and 1 L sterile water, and adjusting the pH to 7.2 with NaOH (1 mol/L). The solid LB culture medium needs another 1.5 g agar for 100 mL liquid. Initially, seed solution of bacteria was transferred to 5 mL liquid LB culture medium and incubated at 37 °C overnight. Then, cBSA-AuAgNCs at predetermined concentration (100 μL) and diluted bacterial suspension (100 μL, $10^6$ CFU/mL) were mixed. The solution was then incubated at 37 °C for 4 h. Three parallel samples were set for each concentration and negative control samples were prepared without adding cBSA-AuAgNCs. Afterwards, the solution was diluted $10^3$ times and spread onto an agar plate. All the plates were incubated under 37 °C and collected after 18 h. The number of grown colonies was counted and compared.

### 2.6 *In vitro* antimicrobial effect

Bacteria-infected Raw 264.7 cells were prepared as model systems to examine the antimicrobial effect of cBSA-AuAgNCs. RAW 264.7 cells (around $10^5$ cells/mL) were incubated in full DMEM medium at 37 °C for 24 h. Next, the medium was removed and the remaining cells were washed with phosphate buffered saline (PBS, pH 7.4). Then fresh DMEM containing bacteria ($10^6$ CFU/mL) was added and the mixture was incubated for another 4 h at 37 °C. Afterwards, the medium was removed and the remaining cells were washed. Subsequently, cells were incubated with DMEM containing cBSA-AuAgNCs (100 μg/mL for *E. coli* and 200 μg/mL for *S. aureus*) for another 4 h. Furthermore, the infected macrophages treated with only DMEM were used as a control. Then 100 μL diluted (10 times) bacteria-infected cell suspension without or with the treatment of cBSA-AuAgNCs was plated onto agar plates, and incubated at 37 °C. The number of bacterial colonies was counted after 18 h.

### 2.7 Drug resistance test

For drug resistance test, M9 culture medium was prepared by mixing 0.5 mL $MgSO_4$ solution (1 mol/L), 2.5 mL $CaCl_2$ solution (10 mmol/L), 50 mL saline solution (1.695 g $Na_2HPO_4$, 0.75 g $KH_2PO_4$, 0.125 g NaCl, and 0.25 g $NH_4Cl$), 2.5 mL 20% glucose, and 200 mL sterile water. The primary minimum inhibitory concentration (MIC) of cBSA-AuAgNCs against *P. aeruginosa* was determined as follows. Different concentrations of cBSA-AuAgNCs (100 μL) and diluted bacterial suspension (100 μL, $10^6$ CFU/mL) were mixed in the 96-well culture plate, which was then incubated at 37 °C for 12 h. The MIC values are defined as the lowest concentration of cBSA-AuAgNCs that can completely inhibit the visible growth of bacteria. Three parallel samples were set for each concentration, and negative control samples were prepared without adding cBSA-AuAgNCs. Then, *P. aeruginosa* was collected from the well contained cBSA-AuAgNCs at a concentration of 1/2 MIC before re-grown in the M9 culture medium at 37 °C. The new bacteria solution (approximately $5 \times 10^6$ CFU/mL) was used to obtain updated MIC values. The experiment was repeated for 21 successive passages. As a control, similar experiments were also performed by using a common antibiotic, gentamicin.

### 2.8 Investigation of AuAgNC–bacteria interactions by confocal imaging

The affinity of bacteria with AuAgNCs was investigated as follows. *E. coli* ($OD_{600}$ = 0.4) was collected and incubated with PBS (pH 7.4), BSA-AuAgNCs (500 μg/mL), or cBSA-AuAgNCs (500 μg/mL) for 1 h under 37 °C. Then the bacteria were isolated by centrifugation and washed. Afterwards, collected bacteria were stained by Hoechst 33342 (diluted with PBS, 1:1,000) for 30 min under 37 °C in dark before observed by confocal microscopy. The signal of Hoechst 33342 was excited by 405 nm and collected in the range of 425–470 nm, while the signal of AuAgNCs was excited by 405 nm and collected in the range of 650–795 nm.

For observing the antimicrobial process, bacteria ($OD_{600}$ = 0.4) were collected and incubated with cBSA-AuAgNCs (0.5 mg/mL for *E. coli* and 1 mg/mL for *S. aureus*) for different time (0.5, 1, 2, and 4 h) under 37 °C. Then the bacteria were isolated by centrifugation and washed. Afterwards, collected bacteria were stained by Nile red (1 μM) for 20 min under 37 °C in dark before observed by confocal microscopy. The signal of Nile red was excited by 552 nm and collected in the range of 580–620 nm. Image J was used to analyze the fluorescence intensity of the confocal images.

### 2.9 Live/dead staining experiment

Hoechst 33342 and PI were used to stain all bacteria and dead bacteria, respectively. Bacteria ($OD_{600}$ = 0.4) were collected and incubated with or without cBSA-AuAgNCs (0.5 mg/mL for *E. coli* and 1 mg/mL for *S. aureus*) for 4 h under 37 °C. Then the bacteria were isolated by centrifugation and washed. Collected bacteria were incubated with Hoechst 33342 and PI (both diluted with PBS, 1:1,000) for 30 min under 37 °C in dark before observed by confocal microscopy. The signal of Hoechst 33342 was excited by 405 nm and collected in the range of 425–470 nm, while the signal of PI was excited by 552 nm and collected in the range of 600–650 nm.

### 2.10 SEM analysis

The morphology of bacteria was observed by SEM. Bacteria were collected ($OD_{600}$ = 0.4) and treated with PBS, BSA-AuAgNCs, or cBSA-AuAgNCs (0.5 mg/mL for *E. coli* and 1 mg/mL for *S. aureus*) under 37 °C for 4 h. Then the treated bacteria were collected by centrifugation and washed before fixed by 2.5% glutaraldehyde under 4 °C for 1 h. Next, the bacteria were washed by water and PBS before dehydrated with different concentrations of ethanol (10%, 30%, 50%, 70%, 90%, and 100%), and then the solution was dropped onto the silicon wafer and dried. Samples were subjected to pre-spray gold treatment before observation by SEM.

### 2.11 ROS test

The bacterial ROS level was measured by a ROS test kit based on 2',7'-dichlorodihydrofluorescein diacetate (DCFH-DA). Bacteria were collected ($OD_{600}$ = 0.4) and re-suspended in PBS. cBSA-AuAgNCs (0.5 mg/mL for *E. coli* and 1 mg/mL for *S. aureus*) were added to the bacteria solution which had been incubated with DCFH-DA (diluted with PBS, 1:1,000) for 1 h under 37 °C. The solution was measured by spectrofluorometer after 30 min. The samples were excited by 480 nm and the fluorescence intensity was collected at 525 nm.

## 3 Results and discussion

### 3.1 Synthesis and characterization of cBSA-AuAgNCs

Cationic cBSA-AuAgNCs were synthesized via the strategy as illustrated in Fig. 1(a). First, fluorescent AuAgNCs were prepared via the biomineralization approach by using BSA as the bio-template owing to its good biocompatibility and abundant surface groups [33, 34]. Afterwards, ethylenediamine was introduced to chemically engineer the surface of AuAgNCs to be cationic according to the previous strategy [35]. Spectral characterization showed that cBSA-AuAgNCs possess featureless absorption in the visible region (Fig. S1 in the Electronic Supplementary Material (ESM)), similar to most reported metal NCs. Meanwhile, cBSA-AuAgNCs exhibit strong fluorescence in the NIR spectral region with the emission maximum at 702 nm (Fig. 1(b)), and the fluorescence intensity is increased slightly compared with that before the modification with ethylenediamine (BSA-AuAgNCs, Fig. S2 in the ESM). Herein, the NIR emission feature makes cBSA-AuAgNCs attractive probes for biological imaging applications [36, 37]. Moreover, the fluorescence lifetime of AuAgNCs was measured upon excitation at 400 nm, and the decay curve was fitted by the bi-exponential function. As shown in Fig. S3 in the ESM, cBSA-AuAgNCs possess an average fluorescence lifetime of 2.52 ± 0.11 μs, which is also slightly longer than that of BSA-AuAgNCs (2.04 ± 0.08 μs). The enhanced fluorescence property of cBSA-AuAgNCs is likely because the introduced electron-rich amine groups have strong electron-donating capability, which is known to facilitate the luminescence generation of metal NCs [38, 39].

TEM was further employed to characterize the size of cBSA-AuAgNCs. As shown in Fig. 1(c), cBSA-AuAgNCs are well dispersed and the average diameter was measured to be 1.8 ± 0.4 nm, which is almost identical to that of BSA-AuAgNCs before the surface modification (Fig. S4 in the ESM). However, the hydrodynamic size of cBSA-AuAgNCs is 8.1 ± 0.5 nm (Fig. 1(d)), which is much larger than that of BSA-AuAgNCs (4.7 ± 0.1 nm), as expected from the additional chemical moieties added to the

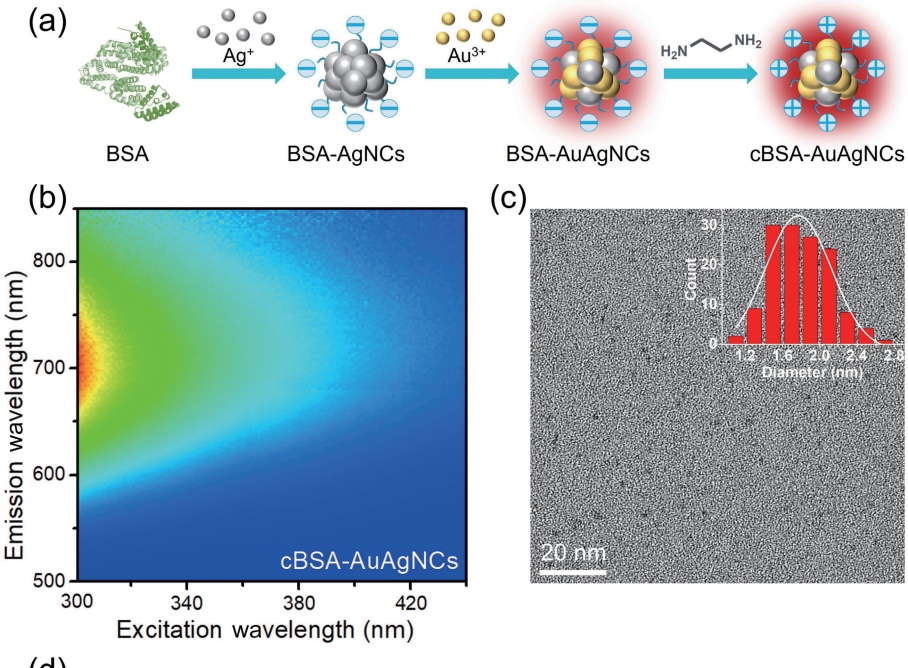


(d)

| Sample | Lifetime (μs) | Core size (nm) | Hydrodynamic size (nm) | Zeta potential (mV) |
|---|---|---|---|---|
| BSA-AuAgNCs | 2.04 ± 0.08 | 1.8 ± 0.5 | 4.7 ± 0.1 | −38.5 ± 1.5 |
| cBSA-AuAgNCs | 2.52 ± 0.11 | 1.8 ± 0.4 | 8.1 ± 0.5 | 37.9 ± 2.2 |

**Figure 1** (a) Schematic illustration of the synthesis of cBSA-AuAgNCs. (b) Two-dimensional (2D) fluorescence profile of cBSA-AuAgNCs in aqueous solution. (c) TEM image of cBSA-AuAgNCs. The inset is the size histogram of cBSA-AuAgNCs obtained from TEM image. (d) Characterization results of BSA-AuAgNCs and cBSA-AuAgNCs.

amino acid side chains. The chemical state of Ag and Au in the as-prepared AuAgNCs was examined by XPS (Figs. 2(a) and 2(b)). In cBSA-AuAgNCs, the binding energy of Ag $3d_{5/2}$ and Ag $3d_{3/2}$ is 368.3 and 374.5 eV, respectively, while the binding energy of Au $4f_{7/2}$ and $4f_{5/2}$ is 83.9 and 87.4 eV, respectively (Table S1 in the ESM). These results indicate that the core components of cBSA-AuAgNCs are mainly metallic Ag(0) and Au(0). Further characterization by inductively coupled plasma optical emission spectrometry (ICP-OES) showed that as-prepared cBSA-AuAgNCs are composed of Au and Ag with a molar ratio of 1.7 (Table S1 in the ESM). We note that while the molar ratio of Au to Ag can be easily modulated by controlling the feeding amount of metal precursors in the synthesis, the present composition was chosen in the following study mainly because it exhibited optimal fluorescence properties that are favorable for further imaging applications (Fig. S5 in the ESM). Precipitate would appear during the reaction if the feeding amount of Au was too high.

The surface charge of as-prepared AuAgNCs was further analyzed (Fig. 1(d)). As expected, the zeta-potential of cBSA-AuAgNCs is highly positive with a value of 37.9 ± 2.2 mV. In contrast, BSA-AuAgNCs possess strong negative charges, with a zeta potential of −38.5 ± 1.5 mV, further confirming the successful modification by ethylenediamine. The abundant positive charges on the surface of cBSA-AuAgNCs make them promising for potential antibacterial and gene delivery applications [40–42]. Furthermore, we examined the stability of cBSA-AuAgNCs by monitoring their fluorescence intensity and zeta potential in aqueous solution under different pH (Fig. S6 in the ESM). As shown, cBSA-AuAgNCs maintained strong NIR fluorescence and positive charges in the physiological pH range of 4.5–9, which are favorable for their further biological application. Moreover, cytotoxicity of cBSA-AuAgNCs towards L929 cells and Raw 264.7 cells was evaluated by applying CCK-8 assay. As shown in Figs. 2(c) and 2(d), with concentrations ranging from 0 to 200 μg/mL, the cell viability was all beyond 80%, which indicates low cytotoxicity of these cBSA-AuAgNCs. Taken together, our characterization showed that these cationic cBSA-AuAgNCs possess NIR fluorescence, abundant positive charges, and low cytotoxicity.

### 3.2 Antimicrobial activity of cBSA-AuAgNCs

To evaluate the antimicrobial activity of cBSA-AuAgNCs, the agar plate experiments for *E. coli* (representative Gram-negative bacteria) and *S. aureus* (representative Gram-positive bacteria) were carried out. As shown in Fig. 3, with the treatment of 2.5 μg/mL cBSA-AuAgNCs to *E. coli*, the number of colonies significantly decreased by 99% compared with the control group. When further increasing the concentration of cBSA-AuAgNCs to 5 μg/mL, almost no bacterial colony was observed. Similar phenomenon appeared in the treatment of cBSA-AuAgNCs against *S. aureus*, suggesting a remarkable antibacterial effect of cBSA-AuAgNCs against both Gram-negative and Gram-positive bacteria. The difference in the antimicrobial activity between two bacteria could be explained by the denser cell walls of Gram-positive bacteria. In stark contrast, BSA-AuAgNC-treated groups did not exhibit obvious antibacterial effect, even under a much higher concentration up to 100 μg/mL (Figs. 3(c) and 3(d) and Fig. S7 in the ESM). Recent studies underscore the important role of surface ligands on the antibacterial activity of metal NCs [43]. Herein, the remarkable difference in the antibacterial features between cBSA-AuAgNCs and BSA-AuAgNCs mostly originates from their different surface charges, and positive charges are apparently favorable for boosting the bactericidal property of these NCs.

In order to evaluate the drug resistance of these cBSA-AuAgNCs, we next investigated their long-term response to *P. aeruginosa*, with gentamicin as the control. The initial MICs of gentamicin and cBSA-AuAgNCs towards *P. aeruginosa* were 0.5 and 5 μg/mL, respectively. As shown in Fig. S8 in the ESM, an obvious increase of the MIC value was observed for gentamicin in the 7th generation, and the value increased ca. 50-fold after 21 passages, which represents a typical drug resistance behavior for traditional antibiotics. In contrast, cBSA-AuAgNCs did not show any obvious drug resistance of *P. aeruginosa*, as seen by the essentially unchanged MIC values during 21 passages. The underlying reason is related with their difference of antibacterial mechanisms, and cationic materials typically can disrupt the membrane of bacteria via strong electrostatic interactions [19, 20,

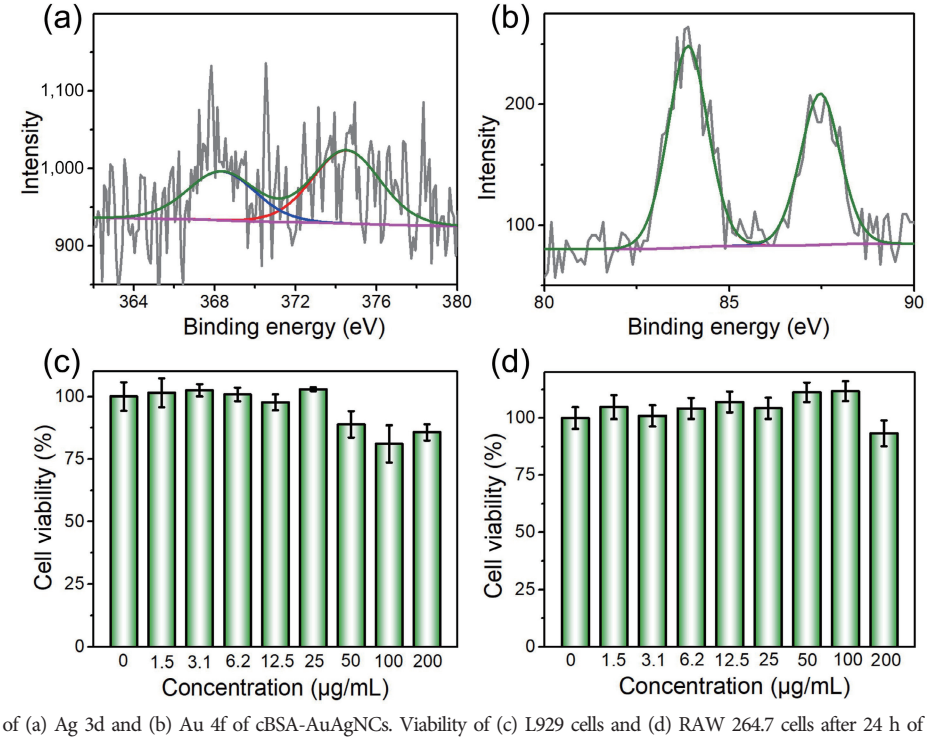


**Figure 2** XPS spectra of (a) Ag 3d and (b) Au 4f of cBSA-AuAgNCs. Viability of (c) L929 cells and (d) RAW 264.7 cells after 24 h of incubation with different concentrations of cBSA-AuAgNCs in the cell medium determined by CCK-8 assay. The error bars mean variations among four separate measurements.

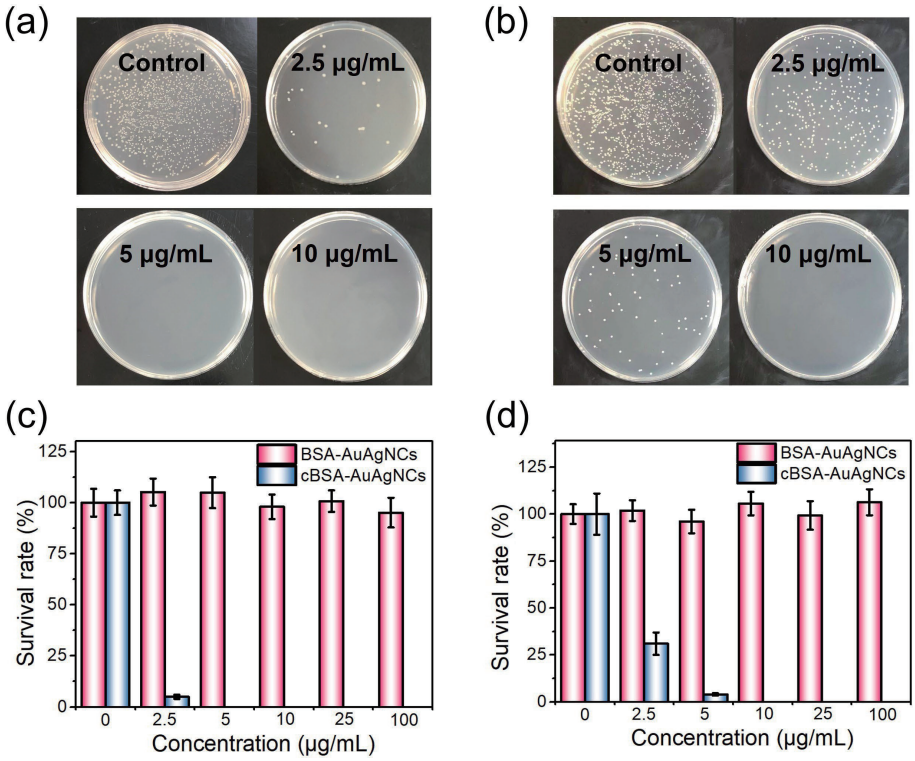


**Figure 3** Photographs of bacterial colonies of (a) *E. coli* and (b) *S. aureus* in the presence of cBSA-AuAgNCs. (c) and (d) Survival rates of *E. coli* and *S. aureus* in the presence of cBSA-AuAgNCs and BSA-AuAgNCs, respectively. The error bars mean variations among three separate measurements.

44]. Moreover, unlike the small antibiotic molecules, nanoagents could kill bacteria through a synergistic effect of multiple mechanisms, which will less likely develop drug resistance [10, 11].

Considering the importance of mononuclear phagocyte system to combat outer pathogens, we further examined the *in vitro* antimicrobial effect of cBSA-AuAgNCs with bacteria-infected macrophages as the model system (Fig. 4(a)). A safe dose of AuAgNCs, based on the cell viability test, was added to RAW 264.7 cells after the infection with *E. coli* and *S. aureus*. Results from the spread plate method showed that the number of bacterial colonies in cBSA-AuAgNC-treated group (Figs. 4(c) and 4(e)) significantly decreased compared with the control group (Figs. 4(b) and 4(d)), with over 90% of bacteria killed. This fact suggests strong antimicrobial ability of cBSA-AuAgNCs inside the macrophage cells.

### 3.3 Interactions between bacteria and cBSA-AuAgNCs

To elucidate the mechanism underlying this significant antibacterial feature of cBSA-AuAgNCs, we employed fluorescence confocal microscopy to investigate their interactions with bacteria. As seen in Fig. 5, similar to the control group, where the bacteria were stained with blue-emitting Hoechst 33342 (blue), no red fluorescence signal from NCs can be observed in the BSA-AuAgNCs group (Fig. 5(e)), suggesting a weak binding of negatively-charged NCs with bacteria. In contrast, strong red fluorescence from cBSA-AuAgNCs can be observed in Fig. 5(h), which indicates a much stronger binding affinity with bacteria than that of BSA-AuAgNCs (Fig. 5(i)). As many other biological systems, the surface of bacteria typically possesses negative charges that will facilitate the binding to cationic materials. Consequently, these cBSA-AuAgNCs can pose strong interactions with the bacteria surface, which is also an important step for further initiating their bactericidal action. Indeed, as shown in Fig. 3, the antibacterial activity of cBSA-AuAgNCs was much higher than that of BSA-AuAgNCs, underlying the importance of interactions with bacterial membranes during the antibacterial process.

By utilizing the intrinsic NIR fluorescence of cBSA-AuAgNCs, we further monitored their antimicrobial process in real time by fluorescence imaging, where the bacterial membrane was also fluorescently stained. As seen in Fig. 6, obvious fluorescence of cBSA-AuAgNCs was observed on the cell membrane after 0.5 h exposure, suggesting the occurrence of interactions between cBSA-AuAgNCs and the membrane of *E. coli*. This phenomenon is similar to the early stage of negatively-charged AuNCs where they were found to accumulate on the cell membrane before the internalization [26, 45]. However, as the time evolved, these cationic cBSA-AuAgNCs were observed to remain stably attached on the bacterial membrane, and much weaker fluorescence appeared inside the cells (Fig. 7). As a matter of fact, the red fluorescence signal of cBSA-AuAgNCs was still observable in the membrane region even after incubation with *E. coli* for 4 h, the time point at which the bacteria were already killed as confirmed by the agar plate experiments. Similar behavior was also observed in the interactions between cBSA-AuAgNCs and Gram-positive bacteria, *S. aureus* (Fig. S9 in the ESM). This fact means that cBSA-AuAgNCs mostly anchored on the outer membrane of bacteria without obvious internalization into cells during the antibacterial process, which is significantly different from the bacterial interactions of negatively-charged metal NCs. In previous studies, Xie et al. [15, 45] found that the internalization of negatively-charged AuNCs by the bacteria is an important prerequisite for their bacterial killing. Herein, our imaging results vividly demonstrated that for cationic antibacterial agents, such as cBSA-AuAgNCs, they can exert strong antimicrobial effects without being internalized into the interior of bacteria. Instead, it is likely strong electrostatic interactions between metal NCs and the bacterial membrane are sufficient to cause the bacterial killing, e.g., via disrupting the membrane integrity and leveraging the ROS levels (as seen below).

To further understand the above observation in fluorescence imaging, live/dead bacterial staining was performed to evaluate the membrane integrity of bacteria upon treatment with cBSA-

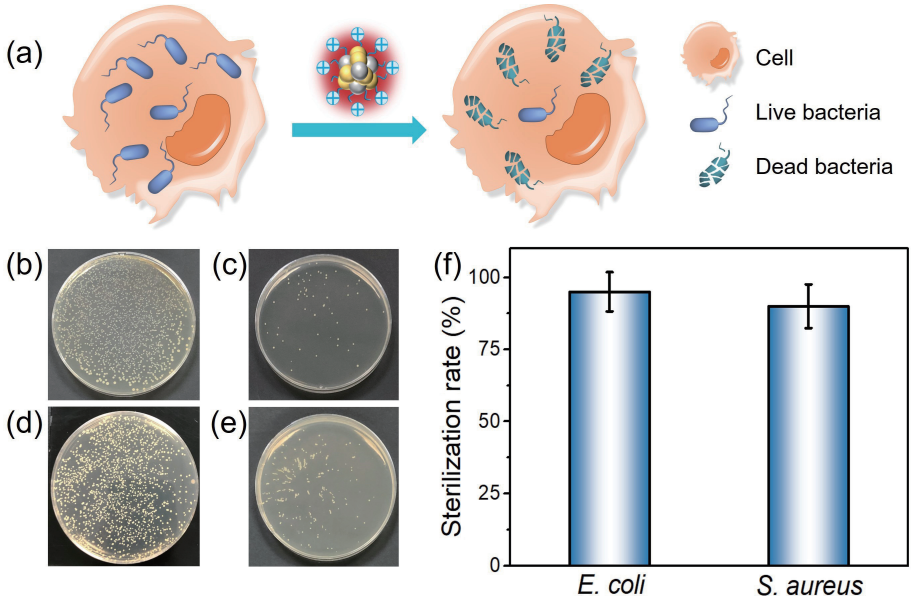


**Figure 4** (a) Schematic illustration of cells infected by bacteria before and after the treatment of cBSA-AuAgNCs. Photographs of bacterial colonies of ((b) and (c)) *E. coli* and ((d) and (e)) *S. aureus* from RAW 264.7 cells ((b) and (d)) without and ((c) and (e)) with treatment of cBSA-AuAgNCs. (f) Sterilization rates of cBSA-AuAgNCs against the bacteria that infect cells. The error bars mean variations among three separate measurements.

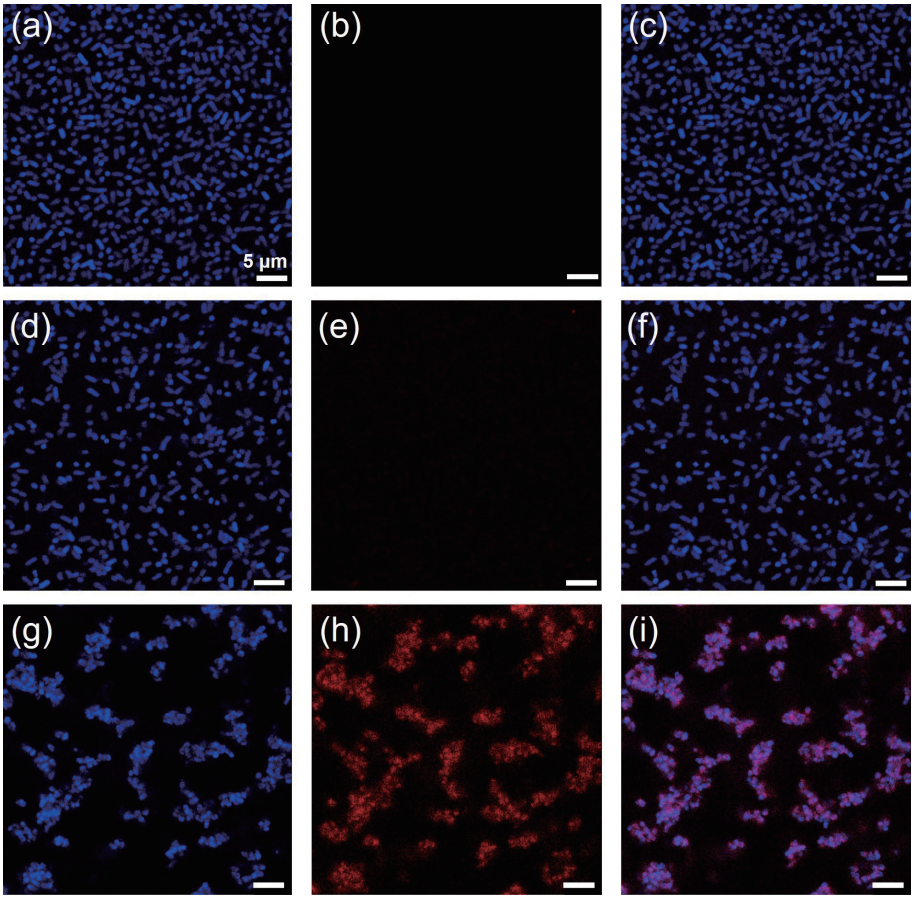


**Figure 5** Confocal fluorescence images of *E. coli* treated with ((a)–(c)) PBS, ((d)–(f)) BSA-AuAgNCs, and ((g)–(i)) cBSA-AuAgNCs. All the bacteria were stained by Hoechst 33342 ((a), (d), and (g), false color: blue). Fluorescent AuAgNCs were assigned as red ((b), (e), and (h)). (c), (f), and (i) are overlay images of blue and red channels. Scale bars are 5 μm.

AuAgNCs. Red fluorescent PI was employed to stain dead bacteria with broken membrane. As shown in Figs. S10 and S11 in the ESM, strong fluorescence of PI can be seen in the samples treated with cBSA-AuAgNCs for both *E. coli* and *S. aureus*, suggesting that the bacterial membranes were indeed ruptured. Further characterization with SEM, as seen in Figs. 8(a)–8(c) and Fig. S12 in the ESM, also confirmed that the surface morphology of bacteria changed dramatically. While the morphology of the bacteria stayed smooth after treated with BSA-AuAgNCs, many nearby bacteria fused together and became wizened in the presence of cBSA-AuAgNCs due to the membrane damage. As a consequence of the membrane damage, it can cause over production of ROS according to previous reports [46, 47]. Thus, we used a fluorescence probe, DCFH-DA, to further investigate the accumulation of ROS in the bacteria triggered by cBSA-AuAgNCs. As shown in Fig. 8(d) and Fig. S13 in the ESM, cBSA-

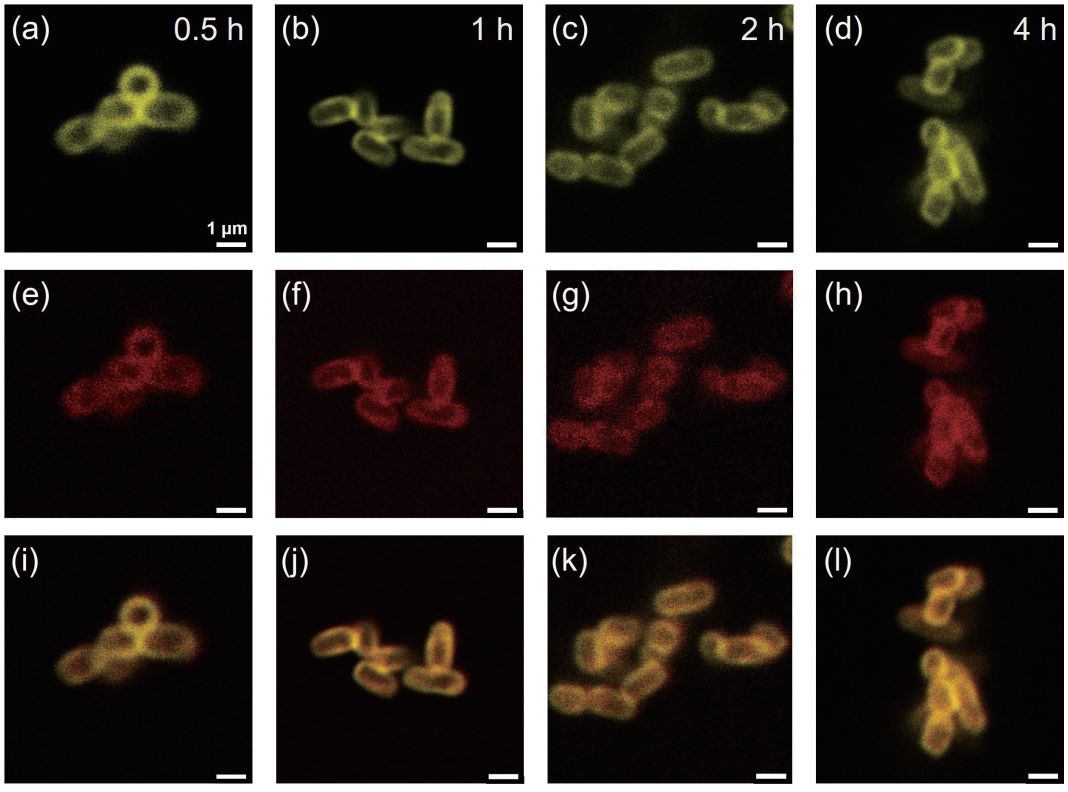


**Figure 6** Confocal fluorescence images of *E. coli* treated with cBSA-AuAgNCs at different time: ((a), (e), and (i)) 0.5 h, ((b), (f), and (j)) 1 h, ((c), (g), and (k)) 2 h, and ((d), (h), and (l)) 4 h. The membrane of bacteria was stained by Nile red ((a)–(d), false color: yellow). Fluorescent cBSA-AuAgNCs were assigned as red ((e)–(h)). (i)–(l) are merged images of both channels. Scale bars are 1 μm.

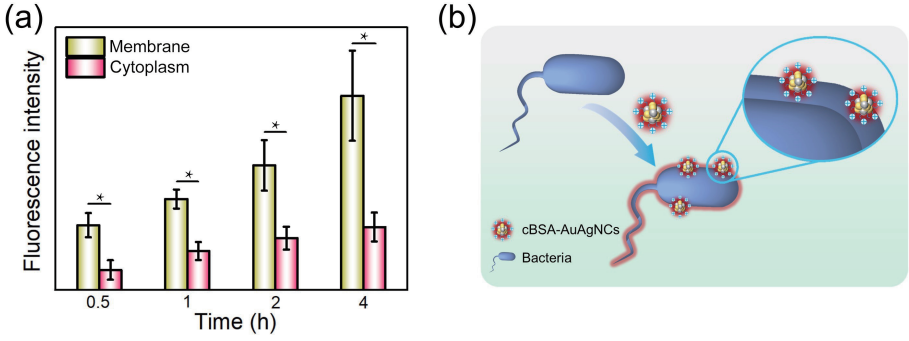


**Figure 7** (a) Statistics of the fluorescence intensity of AuAgNCs in the region of membrane and cytoplasm of *E. coli*. Error bars are the statistic results of over 10 bacteria. * means significant differences within the groups, $p < 0.05$. (b) Schematic illustration of the AuAgNC–bacteria interactions.

AuAgNCs caused ca. 8-fold and 10-fold increase of intracellular ROS compared with the control group for *E. coli* and *S. aureus*, respectively. In contrast, much less increase of intracellular ROS was obtained in the BSA-AuAgNC group, which was not sufficient to cause significant damage to bacteria. Taken these results together with the real time observation from confocal imaging, we propose a possible antibacterial mechanism of these cBSA-AuAgNCs, as illustrated in Fig. 8(e). Unlike negatively-charged metal NCs, these positively-charged AuAgNCs will mostly stick to the surface of bacterial membrane without significant occurrence of cellular internalization. Consequently, the bacterial membrane is seriously disrupted due to strong electrostatic interactions, which then lead to over accumulation of ROS that finally causes the bacterial killing.

## 4 Conclusion

In summary, we have successfully synthesized cationic fluorescent cBSA-AuAgNCs, which possess many interesting characteristics, such as bright NIR fluorescence, strong antibacterial activity, and good biocompatibility. Importantly, the unique fluorescence property of cBSA-AuAgNCs allows the direct observation of their interactions with the bacterial by real time fluorescence imaging. Further quantitative analysis and mechanistic studies revealed that these positively-charged AuAgNCs primarily attached on the bacterial membranes to trigger the subsequent antibacterial process owing to strong electrostatic interactions. Unlike negatively-charged metal NCs, internalization by bacterial cells seems to be unimportant when acting on the bacteria for these cationic agents. Our results demonstrated that cationic luminescent metal NCs can not only act as novel antimicrobial agents, but also serve as a powerful tool for tracing the biological interactions at the nano–bio interfaces in a simple and real time manner.

## Acknowledgements

This work was supported by the National Youth Talents Programme, the Natural Science Foundation of Chongqing (No. cstc2021jcyj-msxmX0980), and the Research Fund of the State Key Laboratory of Solidification Processing (NPU, No. 2020-QZ-01).

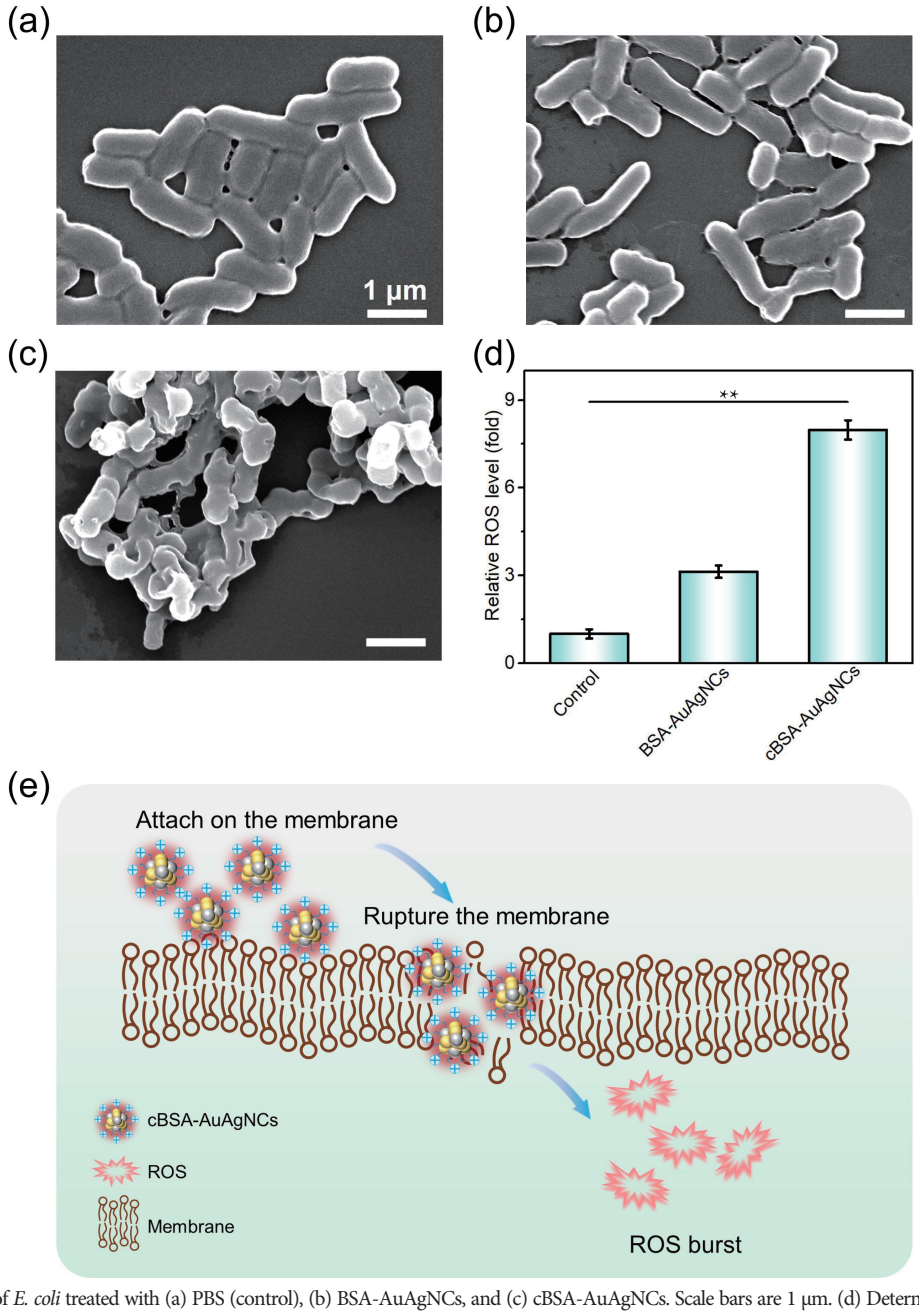


**Figure 8** SEM images of *E. coli* treated with (a) PBS (control), (b) BSA-AuAgNCs, and (c) cBSA-AuAgNCs. Scale bars are 1 μm. (d) Determination of ROS in *E. coli* solution by using DCFH-DA dye. The error bars mean variations among three separate measurements. ** means extreme significant difference against the control group, $p < 0.01$. (e) Proposed antibacterial mechanism of cBSA-AuAgNCs.

**Electronic Supplementary Material:** Supplementary material (additional data on AuAgNCs characterization, antimicrobial experiments, confocal images, and SEM images) is available in the online version of this article at https://doi.org/10.1007/s12274-022-4837-x.

## References

[1] Vasilev, K.; Sah, V.; Anselme, K.; Ndi, C.; Mateescu, M.; Dollmann, B.; Martinek, P.; Ys, H.; Ploux, L.; Griesser, H. J. Tunable antibacterial coatings that support mammalian cell growth. *Nano Lett.* **2010**, *10*, 202–207.

[2] Qiu, H.; Pu, F.; Liu, Z. W.; Liu, X. M.; Dong, K.; Liu, C. Q.; Ren, J. S.; Qu, X. G. Hydrogel-based artificial enzyme for combating bacteria and accelerating wound healing. *Nano Res.* **2020**, *13*, 496–502.

[3] Neu, H. C. The crisis in antibiotic resistance. *Science* **1992**, *257*, 1064–1073.

[4] Levy, S. B.; Marshall, B. Antibacterial resistance worldwide: Causes, challenges and responses. *Nat. Med.* **2004**, *10*, S122–S129.

[5] Chen, X. K.; Zhang, X. D.; Lin, F. M.; Guo, Y. X.; Wu, F. G. One-step synthesis of epoxy group-terminated organosilica nanodots: A versatile nanoplatform for imaging and eliminating multidrug-resistant bacteria and their biofilms. *Small* **2019**, *15*, 1901647.

[6] Mei, L.; Lu, Z. T.; Zhang, X. E.; Li, C. X.; Jia, Y. X. Polymer-Ag nanocomposites with enhanced antimicrobial activity against bacterial infection. *ACS Appl. Mater. Interfaces* **2014**, *6*, 15813–15821.

[7] Pillai, P. P.; Kowalczyk, B.; Kandere-Grzybowska, K.; Borkowska, M.; Grzybowski, B. A. Engineering Gram selectivity of mixed-charge gold nanoparticles by tuning the balance of surface charges. *Angew. Chem., Int. Ed.* **2016**, *55*, 8610–8614.

[8] Pranantyo, D.; Liu, P.; Zhong, W. B.; Kang, E. T.; Chan-Park, M. B. Antimicrobial peptide-reduced gold nanoclusters with charge-reversal moieties for bacterial targeting and imaging. *Biomacromolecules* **2019**, *20*, 2922–2933.

[9] Yang, J. J.; Zhang, X. D.; Ma, Y. H.; Gao, G.; Chen, X. K.; Jia, H. R.; Li, Y. H.; Chen, Z.; Wu, F. G. Carbon dot-based platform for simultaneous bacterial distinguishment and antibacterial applications. *ACS Appl. Mater. Interfaces* **2016**, *8*, 32170–32181.

[10] Li, D.; Kumari, B.; Makabenta, J. M.; Tao, B. L.; Qian, K.; Mei, X. F.; Rotello, V. M. Development of coinage metal nanoclusters as antimicrobials to combat bacterial infections. *J. Mater. Chem. B* **2020**, *8*, 9466–9480.
[11] Zhao, Y.; Chen, L.; Wang, Y. N.; Song, X. Y.; Li, K. Y.; Yan, X. F.; Yu, L. M.; He, Z. Y. Nanomaterial-based strategies in antimicrobial applications: Progress and perspectives. *Nano Res.* **2021**, *14*, 4417–4441.
[12] Lin, B.; Li, R.; Handley, T. N. G.; Wade, J. D.; Li, W. Y.; O'Brien-Simpson, N. M. Cationic antimicrobial peptides are leading the way to combat oropathogenic infections. *ACS Infect. Dis.* **2021**, *7*, 2959–2970.
[13] Sang, Y. J.; Li, W.; Liu, H.; Zhang, L.; Wang, H.; Liu, Z. W.; Ren, J. S.; Qu, X. G. Construction of nanozyme-hydrogel for enhanced capture and elimination of bacteria. *Adv. Funct. Mater.* **2019**, *29*, 1900518.
[14] Hayden, S. C.; Zhao, G. X.; Saha, K.; Phillips, R. L.; Li, X. N.; Miranda, O. R.; Rotello, V. M.; El-Sayed, M. A.; Schmidt-Krey, I.; Bunz, U. H. F. Aggregation and interaction of cationic nanoparticles on bacterial surfaces. *J. Am. Chem. Soc.* **2012**, *134*, 6920–6923.
[15] Zheng, K. Y.; Setyawati, M. I.; Leong, D. T.; Xie, J. P. Antimicrobial gold nanoclusters. *ACS Nano* **2017**, *11*, 6904–6910.
[16] Zheng, K. Y.; Xie, J. P. Cluster materials as traceable antibacterial agents. *Acc. Mater. Res.* **2021**, *2*, 1104–1116.
[17] Yougbare, S.; Chang, T. K.; Tan, S. H.; Kuo, J. C.; Hsu, P. H.; Su, C. Y.; Kuo, T. R. Antimicrobial gold nanoclusters: Recent developments and future perspectives. *Int. J. Mol. Sci.* **2019**, *20*, 2924.
[18] Wang, Z. P.; Fang, Y. S.; Zhou, X. F.; Li, Z. B.; Zhu, H. G.; Du, F. L.; Yuan, X.; Yao, Q. F.; Xie, J. P. Embedding ultrasmall Ag nanoclusters in Luria-Bertani extract via light irradiation for enhanced antibacterial activity. *Nano Res.* **2020**, *13*, 203–208.
[19] Li, Y. X.; Zhen, J. B.; Tian, Q.; Shen, C. Q.; Zhang, L. B.; Yang, K. W.; Shang, L. One step synthesis of positively charged gold nanoclusters as effective antimicrobial nanoagents against multidrug-resistant bacteria and biofilms. *J. Colloid Interface Sci.* **2020**, *569*, 235–243.
[20] Xie, Y. Z. Y.; Liu, Y.; Yang, J. C.; Liu, Y.; Hu, F. P.; Zhu, K.; Jiang, X. Y. Gold nanoclusters for targeting methicillin-resistant staphylococcus aureus *in vivo*. *Angew. Chem., Int. Ed.* **2018**, *57*, 3958–3962.
[21] Mi, W. Y.; Tang, S.; Guo, S. S.; Li, H. J.; Shao, N. *In situ* synthesis of red fluorescent gold nanoclusters with enzyme-like activity for oxidative stress amplification in chemodynamic therapy. *Chin. Chem. Lett.* **2022**, *33*, 1331–1336.
[22] Zheng, Y. K.; Wu, J. B.; Jiang, H.; Wang, X. M. Gold nanoclusters for theranostic applications. *Coord. Chem. Rev.* **2021**, *431*, 213689.
[23] Qiao, Z. J.; Zhang, J.; Hai, X.; Yan, Y. C.; Song, W. L.; Bi, S. Recent advances in templated synthesis of metal nanoclusters and their applications in biosensing, bioimaging and theranostics. *Biosens. Bioelectron.* **2021**, *176*, 112898.
[24] Shang, L.; Nienhaus, G. U. Research update: Interfacing ultrasmall metal nanoclusters with biological systems. *APL Mater.* **2017**, *5*, 053101.
[25] Su, Y.; Xue, T. T.; Liu, Y. X.; Qi, J. X.; Jin, R. C.; Lin, Z. K. Luminescent metal nanoclusters for biomedical applications. *Nano Res.* **2019**, *12*, 1251–1265.
[26] Yang, L. X.; Shang, L.; Nienhaus, G. U. Mechanistic aspects of fluorescent gold nanocluster internalization by live HeLa cells. *Nanoscale* **2013**, *5*, 1537–1543.
[27] Xu, J.; Shang, L. Emerging applications of near-infrared fluorescent metal nanoclusters for biological imaging. *Chin. Chem. Lett.* **2018**, *29*, 1436–1444.
[28] Liu, H. L.; Hong, G. S.; Luo, Z. T.; Chen, J. C.; Chang, J. L.; Gong, M.; He, H.; Yang, J.; Yuan, X.; Li, L. L. et al. Atomic-precision gold clusters for NIR-II imaging. *Adv. Mater.* **2019**, *31*, 1901015.
[29] Kang, X.; Zhu, M. Z. Tailoring the photoluminescence of atomically precise nanoclusters. *Chem. Soc. Rev.* **2019**, *48*, 2422–2457.
[30] Crawford, S. E.; Hartmann, M. J.; Millstone, J. E. Surface chemistry-mediated near-infrared emission of small coinage metal nanoparticles. *Acc. Chem. Res.* **2019**, *52*, 695–703.
[31] Xiao, Y.; Wu, Z. N.; Yao, Q. F.; Xie, J. P. Luminescent metal nanoclusters: Biosensing strategies and bioimaging applications. *Aggregate* **2021**, *2*, 114–132.
[32] Wang, Z. J.; Li, Q.; Tan, L. L.; Liu, C. G.; Shang, L. Metal-organic frameworks-mediated assembly of gold nanoclusters for sensing applications. *J. Anal. Test.* **2022**, *6*, 163–177.
[33] Nosrati, H.; Sefidi, N.; Sharafi, A.; Danafar, H.; Manjili, H. K. Bovine serum albumin (BSA) coated iron oxide magnetic nanoparticles as biocompatible carriers for curcumin-anticancer drug. *Bioorg. Chem.* **2018**, *76*, 501–509.
[34] Xie, J. P.; Zheng, Y. G.; Ying, J. Y. Protein-directed synthesis of highly fluorescent gold nanoclusters. *J. Am. Chem. Soc.* **2009**, *131*, 888–889.
[35] Zhong, W. C.; Wen, M. Y.; Xu, J.; Wang, H. X.; Tan, L. L.; Shang, L. Simultaneous regulation of optical properties and cellular behaviors of gold nanoclusters by pre-engineering the biotemplates. *Chem. Commun.* **2020**, *56*, 11414–11417.
[36] He, K.; Zhu, J. Y.; Gong, L. S.; Tan, Y.; Chen, H. R.; Liang, H. R.; Huang, B. H.; Liu, J. B. He, K.; Zhu, J. Y.; Gong, L. S.; Tan, Y.; Chen, H. R.; Liang, H. R.; Huang, B. H.; Liu, J. B.. *Nano Res.* **2021**, *14*, 1087–1094.
[37] Zhao, W. B.; Wang, R. T.; Liu, K. K.; Du, M. R.; Wang, Y.; Wang, Y. Q.; Zhou, R.; Liang, Y. C.; Ma, R. N.; Sui, L. Z. et al. Near-infrared carbon nanodots for effective identification and inactivation of Gram-positive bacteria. *Nano Res.* **2022**, *15*, 1699–1708.
[38] Xu, J.; Li, J. M.; Zhong, W. C.; Wen, M. Y.; Sukhorukov, G.; Shang, L. The density of surface ligands regulates the luminescence of thiolated gold nanoclusters and their metal ion response. *Chin. Chem. Lett.* **2021**, *32*, 2390–2394.
[39] Wu, Z. K.; Jin, R. C. On the ligand's role in the fluorescence of gold nanoclusters. *Nano Lett.* **2010**, *10*, 2568–2573.
[40] Wilson, W. W.; Wade, M. M.; Holman, S. C.; Champlin, F. R. Status of methods for assessing bacterial cell surface charge properties based on zeta potential measurements. *J. Microbiol. Methods* **2001**, *43*, 153–164.
[41] Zhang, Y. Q.; Hudson-Smith, N. V.; Frand, S. D.; Cahill, M. S.; Davis, L. S.; Feng, Z. V.; Haynes, C. L.; Hamers, R. J. Influence of the spatial distribution of cationic functional groups at nanoparticle surfaces on bacterial viability and membrane interactions. *J. Am. Chem. Soc.* **2020**, *142*, 10814–10823.
[42] Dutta, D.; Chattopadhyay, A.; Ghosh, S. S. Cationic BSA templated Au-Ag bimetallic nanoclusters as a theranostic gene delivery vector for HeLa cancer cells. *ACS Biomater. Sci. Eng.* **2016**, *2*, 2090–2098.
[43] Zheng, K. Y.; Setyawati, M. I.; Leong, D. T.; Xie, J. P. Surface ligand chemistry of gold nanoclusters determines their antimicrobial ability. *Chem. Mater.* **2018**, *30*, 2800–2808.
[44] Cao, W. W.; Wang, X.; Li, Q.; Peng, X. F.; Wang, L. N.; Li, P. L.; Ye, Z. W.; Xing, X. D. Designing of membrane-active nano-antimicrobials based on cationic copolymer functionalized nanodiamond: Influence of hydrophilic segment on antimicrobial activity and selectivity. *Mater. Sci. Eng. C* **2018**, *92*, 307–316.
[45] Zheng, K. Y.; Setyawati, M. I.; Leong, D. T.; Xie, J. P. Observing antimicrobial process with traceable gold nanoclusters. *Nano Res.* **2021**, *14*, 1026–1033.
[46] Zheng, K. Y.; Setyawati, M. I.; Leong, D. T.; Xie, J. P. Overcoming bacterial physical defenses with molecule-like ultrasmall antimicrobial gold nanoclusters. *Bioact. Mater.* **2021**, *6*, 941–950.
[47] Zhao, Y. Y.; Tian, Y.; Cui, Y.; Liu, W. W.; Ma, W. S.; Jiang, X. Y. Small molecule-capped gold nanoparticles as potent antibacterial agents that target Gram-negative bacteria. *J. Am. Chem. Soc.* **2010**, *132*, 12349–12356.